Finite element micromagnetics

Thomas Schrefl, Dieter Suess, Werner Scholz, Hermann Forster, Vassilios Tsiantos, and Josef Fidler

Vienna University of Technology, Institute of Applied and Technical Physics, Wiedner Hauptstr. 8-10, A-1040 Vienna, Austria

Abstract. The development of advanced magnetic materials such as magnetic sensors, recording heads, and magneto-mechanic devices requires a precise understanding of the magnetic behavior. As the size of the magnetic components approach the nanometer regime, detailed predictions of the magnetic properties becomes possible using micromagnetic simulations. Micromagnetics combines Maxwell's equations for the magnetic field with an equation of motion describing the time evolution of the magnetization. The local arrangement of the magnetic moments follows from the complex interaction between intrinsic magnetic properties such as the magnetocrystalline anisotropy and the physical/chemical microstructure of the material. This paper reviews the basic numerical methods used in finite element micromagnetic simulations and presents numerical examples in the field of soft magnetic sensor elements, polycrystalline thin film elements, and magnetic nanowires.

1 Introduction

Micromagnetism is a continuum theory to describe magnetization processes on a significant length scale which is large enough to replace atomistic magnetic moments by a continuous function of position and small enough to reveal the transitions between magnetic domains [1]. With the rapid increase in computer power, numerical micromagnetics has become an important tool to characterize magnetic materials as used in high density magnetic recording and magneto-electronics [2]. The development of ultrahigh density storage media [3] and magneto-electronic devices [4] requires a precise understanding of the magnetization reversal process. The numerical integration of the equation of motions which describe the dynamic response of a magnetic system under the influence of an external field provides a detailed understanding of the microscopic processes that determine the macroscopic magnetic properties like switching time and switching field. In addition to external parameters like the applied magnetic field and the temperature, the magnetization reversal process significantly depends on the interplay between the physical/chemical microstructure of a magnet and the local arrangement of the magnetic moments.

The finite element method is a highly flexible tool to describe magnetization processes, since it is possible to incorporate the physical grain structure and to adjust the finite element mesh according to the local magnetization.

An efficient a posteriori error indicator can be defined making use of a conservation law inherent to the physics of the problem. In order to treat the magnetostatic interactions of distinct magnetic parts, the finite element method can be combined with a boundary element method. The space discretization of the partial differential equations which describe the magnetization dynamics leads to a stiff system of ordinary differential equations. Preconditioned backward differentiation methods significantly reduce the CPU time as compared to Adams or Runge-Kutta methods for time integration.

The paper is organized as follows. Section 2 introduces the basic set of partial differential equations that describes the time evolution of a magnetic system. Section 3 presents basic numerical techniques used in the simulation of magnetic microstructures. Section 3.1 presents the hybrid finite element / boundary element methods for the calculation of the magnetostatic field. Section 3.2 deals with the time integration of the equation of motion, and section 3.3 briefly discusses an adaptive refinement scheme. Section 4 presents some recent examples of micromagnetic simulations. Section 4a presents magnetostatically driven reversal processes in magnetic nano-dots. Section 4b shows the influence of surface roughness on the magnetization reversal of magnetic nano-elements. Section 4c treats the motion of domains walls in magnetic nano-wires using adaptive mesh refinement.

2 Micromagnetics

2.1 Basic principles of micromagnetism

The basic concept of micromagnetism is to replace the atomic magnetic moments by a continuous function of position. In a continuum theory the local direction of the magnetic moments may be described by the magnetic polarization vector

$$\boldsymbol{J}(\boldsymbol{r}) = \mu_0 \boldsymbol{M}(\boldsymbol{r}) = \mu_0 \boldsymbol{m}/V. \tag{1}$$

The magnetic polarization $\boldsymbol{J}$ is proportional to the magnetization, which is given by the magnetic moment, $\boldsymbol{m}$, per unit volume, V. μ_0 is the magnetic permeability of vacuum. The second principle of micromagnetism treats the magnitude of the magnetization as a function of temperature only. The modulus of $\boldsymbol{J}$,

$$|\boldsymbol{J}| = J_\mathrm{s}(T), \tag{2}$$

is assumed to be a function of temperature and to be independent of the local magnetic field. Thus the magnetic state of the system can be uniquely described by the directions cosines $b_i(\boldsymbol{r})$ of the magnetic polarization, $\boldsymbol{J} = \boldsymbol{b}J_\mathrm{s}$. In a metastable equilibrium state, $\boldsymbol{b}(\boldsymbol{r})$ minimizes the the total Gibbs free energy energy of the system.

2.2 Total magnetic Gibbs free energy

The contributions to the total magnetic Gibbs free energy are derived from classical electrodynamics, condensed matter physics, and quantum mechanics so that the continuous expressions for the energy describe the interactions of the spins with the external field, the crystal lattice, and the interactions of the spins with one another. The latter consists of long-range magnetostatic interactions and short-range quantum-mechanical exchange interactions. The competitive effects of the micromagnetic energy contributions upon minimization determine the equilibrium distribution of the magnetization. The minimization of the ferromagnetic exchange energy aligns the magnetic moments parallel to each other, whereas the minimization of the magnetostatic energy favors the existence of magnetic domains. The magnetocrystalline anisotropy energy describes the interaction of the magnetization with the crystal lattice. Its minimization orients the magnetization preferably along certain crystallographic directions. The minimization of the Zeeman energy of the magnetization in an external field rotates the magnetization parallel to the applied field.

The total magnetic Gibbs free energy, E_t may be written in the following form [5]

$$E_\mathrm{t} = \int_{\Omega_\mathrm{int}} \left\{ -\frac{1}{2}\boldsymbol{H}_\mathbf{d} \cdot \boldsymbol{J} + A\sum_{i=1}^{3}(\nabla b_i)^2 + f_\mathrm{k}(\boldsymbol{b}) - \boldsymbol{H}_\mathbf{app} \cdot \boldsymbol{J} \right\} \mathrm{d}^3 r. \tag{3}$$

In (3) the first term of the integrand is the magnetostatic energy density, the second term is the exchange energy density, the third term denotes the magnetocrystalline anisotropy density, and the last term is the Zeeman energy. The integral extends over the total volume of all magnetic particles, Ω_int. $\boldsymbol{H}_\mathrm{d}$, A, and $\boldsymbol{H}_\mathrm{app}$ denote the demagnetizing field, the exchange constant, and the applied magnetic field, respectively. For uniaxial materials the magnetocrystalline anisotropy density may be written as

$$f_\mathrm{k} = -K_\mathrm{u}(\boldsymbol{u} \cdot \boldsymbol{b})^2, \tag{4}$$

where K_u is the anisotropy constant and $\boldsymbol{u}$ is the unit vector along the easy axis. The intrinsic magnetic properties A, K_u, and J_s and the spatial distribution of the easy axes can be determined experimentally. In a polycrystalline material the direction of the easy axis changes from grain to grain. In addition, the intrinsic magnetic properties may be space dependent.

The demagnetizing field follows from a magnetic scalar potential, U,

$$\boldsymbol{H}_\mathrm{d} = -\nabla U. \tag{5}$$

The scalar potential solves the Poisson equation

$$\triangle U(\boldsymbol{r}) = \frac{\nabla \boldsymbol{J}(\boldsymbol{r})}{\mu_0} \qquad \text{for } \boldsymbol{r} \in \Omega_\mathrm{int} \tag{6}$$

within $\Omega_{\rm int}$, the space occupied by the magnetic particles. Outside the magnetic particles, $\Omega_{\rm ext}$, (6) reduces to the Laplace equation

$$\triangle U(\boldsymbol{r}) = 0 \qquad \text{for } \boldsymbol{r} \in \Omega_{\rm ext}. \tag{7}$$

At the boundary of the magnet Γ the boundary conditions

$$U^{\rm int} = U^{\rm ext}, \;\; \left(\nabla U^{\rm int} - \nabla U^{\rm ext}\right) \cdot \boldsymbol{n} = \frac{\boldsymbol{J} \cdot \boldsymbol{n}}{\mu_0}, \tag{8}$$

hold. Here $\boldsymbol{n}$ denotes the outward pointing normal unit vector on Γ. The magnetic scalar potential is regular at infinity

$$U \propto 1/\boldsymbol{r} \quad \text{for } \boldsymbol{r} \to \infty. \tag{9}$$

The minimization of (3) subjects to the constraints $|\boldsymbol{J}| = J_{\rm s}$, and (6) to (9) provides a metastable equilibrium state of the magnetic system. The subsequent minimization of (3) for different applied field gives the hysteresis curve. Within this static approach, hysteresis is the way the system follows its path through the local minima of the energy landscape [6].

2.3 The Landau-Lifshitz-Gilbert equation

The coercive field of a magnetic is a dynamic property. The measured coercivity significantly depends on the rate of change of the external field. Several experiments show an enhancement of the coercive field with decreasing pulse width of the external field [7]. The dynamic coercivity becomes important in ultra-high density and high data rate magnetic storage [8]. In addition to thermal effects, the gyromagnetic precession causes the increase of the coercive field at short times [9]. The precessional motion of a magnetic moment in the absence of damping is described by the torque equation. According to quantum theory the angular momentum associated with a magnetic moment $\boldsymbol{m}$ is

$$\boldsymbol{L} = \boldsymbol{m}/\gamma, \tag{10}$$

where γ is the gyromagnetic ratio. The torque on the magnetic moment, $\boldsymbol{m}$, exerted by an effective magnetic field, $\boldsymbol{H}_{\rm eff}$,

$$\boldsymbol{T} = \boldsymbol{m} \times \boldsymbol{H}_{\rm eff}. \tag{11}$$

The change of the angular momentum with time equals the torque,

$$\frac{\partial}{\partial t}\left(\frac{\boldsymbol{m}}{\gamma}\right) = \boldsymbol{m} \times \boldsymbol{H}_{\rm eff}, \tag{12}$$

which describes the precession of the magnetic moment around the effective field. In equilibrium the change of the angular momentum with time is zero and thus the torque is zero. In order to describe the motion of the magnetic

moment towards equilibrium a viscous damping term can be included. A dissipative term proportional to the generalized velocity, $(\partial \boldsymbol{m}/\partial t)$, is added to the effective field. With η being a positive constant, the dissipative term $-\eta(\partial \boldsymbol{m}/\partial t)$ slows down the motion of the magnetic moment and aligns $\boldsymbol{m}$ parallel to $\boldsymbol{H}_{\text{eff}}$. This gives the Gilbert equation of motion [10]

$$\frac{\partial \boldsymbol{m}}{\partial t} = -|\gamma| \boldsymbol{m} \times \left(\boldsymbol{H}_{\text{eff}} - \eta \frac{\partial \boldsymbol{m}}{\partial t} \right). \tag{13}$$

Within the framework of a continuum theory (13) has to hold in every point within a ferromagnetic material. Thus we can replace the magnetic moment, $\boldsymbol{m}$, with the magnetic polarization vector, $\boldsymbol{J}$, and write the equation of motion in continuous form

$$\frac{\partial \boldsymbol{J}}{\partial t} = -|\gamma| \boldsymbol{J} \times \boldsymbol{H}_{\text{eff}} + \frac{\alpha}{J_{\text{s}}} \boldsymbol{J} \times \frac{\partial \boldsymbol{J}}{\partial t}. \tag{14}$$

In (14) the dimensionless Gilbert damping constant $\alpha = \gamma \eta J_{\text{s}}$ was introduced. Multiplying (14) with $\boldsymbol{J}\cdot$ shows that the equation of motion conserves the norm of the magnetic polarization vector, since the right hand side vanishes: $\partial \left(\boldsymbol{J} \cdot \boldsymbol{J} \right) / \partial t = \partial J_{\text{s}}^2 / \partial t = 0$. Multiplying both sides of (14) with $\boldsymbol{J}\times$ gives

$$\boldsymbol{J} \times \frac{\partial \boldsymbol{J}}{\partial t} = -|\gamma| \boldsymbol{J} \times (\boldsymbol{J} \times \boldsymbol{H}_{\text{eff}}) + \frac{\alpha}{J_{\text{s}}} \boldsymbol{J} \times \left(\boldsymbol{J} \times \frac{\partial \boldsymbol{J}}{\partial t} \right). \tag{15}$$

Using the $\boldsymbol{a} \times (\boldsymbol{b} \times \boldsymbol{c}) = (\boldsymbol{a} \cdot \boldsymbol{c})\boldsymbol{b} - (\boldsymbol{a} \cdot \boldsymbol{b})\boldsymbol{c}$, we can rewrite (15)

$$\begin{aligned} \boldsymbol{J} \times \frac{\partial \boldsymbol{J}}{\partial t} &= -|\gamma| \boldsymbol{J} \times (\boldsymbol{J} \times \boldsymbol{H}_{\text{eff}}) + \frac{\alpha}{J_{\text{s}}} \left(\boldsymbol{J} \cdot \frac{\partial \boldsymbol{J}}{\partial t} \right) \boldsymbol{J} - \frac{\alpha}{J_{\text{s}}} (\boldsymbol{J} \cdot \boldsymbol{J}) \frac{\partial \boldsymbol{J}}{\partial t}, \\ \boldsymbol{J} \times \frac{\partial \boldsymbol{J}}{\partial t} &= -|\gamma| \boldsymbol{J} \times (\boldsymbol{J} \times \boldsymbol{H}_{\text{eff}}) - \alpha \frac{\partial \boldsymbol{J}}{\partial t}. \end{aligned} \tag{16}$$

If we substitute this result into (14), we obtain the Landau-Lifshitz-Gilbert equation

$$\frac{\partial \boldsymbol{J}}{\partial t} = -\frac{|\gamma|}{1+\alpha^2} \boldsymbol{J} \times \boldsymbol{H}_{\text{eff}} - \frac{|\gamma| \alpha}{(1+\alpha^2) J_{\text{s}}} \boldsymbol{J} \times (\boldsymbol{J} \times \boldsymbol{H}_{\text{eff}}). \tag{17}$$

The effective field,

$$\boldsymbol{H}_{\text{eff}} = -\frac{\delta E_{\text{t}}}{\delta \boldsymbol{J}}, \tag{18}$$

is the negative variational derivative of the total magnetic Gibbs free energy. Each energy term contributes to the effective field. The different contributions to the effective field are the demagnetzing field, $\boldsymbol{H}_{\text{d}}$, the exchange field, $\boldsymbol{H}_{\text{ex}}$ the anisotropy field, $\boldsymbol{H}_{\text{K}}$, and the applied field, $\boldsymbol{H}_{\text{app}}$. Whereas the anisotropy field depends only locally on the magnetic polarization, the exchange field and the demagnetizing field account for interactions. The exchange interactions

are short range. The magnetostatic interactions are long range, since the magnetic potential U depends on the magnetic volume charges, $\nabla \cdot \boldsymbol{J}/\mu_0$, and magnetic surface charges, $\boldsymbol{J} \cdot \boldsymbol{n}/\mu_0$, over all magnetic particles. The variation of the exchange energy gives the exchange field

$$\boldsymbol{H}_{\mathrm{ex}} = \frac{2A}{J_{\mathrm{s}}} \triangle \boldsymbol{b}. \tag{19}$$

The LLG equation (17) is a partial differential equation which is coupled to the magnetostatic boundary value problem (6) to (9).

3 Numerical methods

3.1 Magnetostatics

A key part in micromagnetic simulations is the calculation of the magnetic field which arises from the interaction of the magnetization with the element geometry. This so-called demagnetizing field is crucial for the formation of the magnetic domain structure in large elements and determines the external field required to reverse the magnetization of small elements. The magnetostatic interactions between distinct magnetic elements become important in magnetic multilayers or arrays of magnetic dots used for sensor applications, and magnetic storage.

The partial differential equations for the magnetic scalar potential (6) to (9) define an open boundary problem. The potential or its normal derivative are only know at infinity. In principle one has to mesh a wide region outside the magnetic particles in order to account for the boundary conditions at infinity (9). In order to overcome these problems various techniques to treat open boundaries in finite element simulations have been proposed [11]. A hybrid finite element/boundary element method originally introduced by Fredkin and Koehler [12] is very suitable for micromagnetic simulations, as it treats the magnetostatic interactions between distinct magnetic parts without the need to mesh the space outside the magnetic bodies. This feature becomes important simulating the magnetostatic interactions between sensors elements or the writing process in magnetic recording.

The basic concept of this approach is to split the calculations into to parts using the superposition principle. First a potential, U_1, which arises from the magnetic charges within the individual magnetic bodies is calculated. In a second step, a potential, U_2, which accounts for the magnetostatic interactions between distinct bodies and the boundary conditions at infinity, is calculated. The potential U_1 is assumed to solve a closed boundary value problem. Then the equations for U_2 can be derived from (6)–(9), which hold for the total potential $U = U_1 + U_2$. The potential U_1 can be computed from the closed boundary value problem,

$$\triangle U_1(\boldsymbol{r}) = \frac{\nabla \cdot \boldsymbol{J}(\boldsymbol{r})}{\mu_0} \quad \text{for } \boldsymbol{r} \in \Omega_{\mathrm{int}} \tag{20}$$

$$U_1 = 0 \qquad \text{for } \boldsymbol{r} \in \Omega_{\text{ext}} \tag{21}$$

$$\nabla U_1 \cdot \boldsymbol{n} = \frac{\boldsymbol{J} \cdot \boldsymbol{n}}{\mu_0} \qquad \text{for } \boldsymbol{r} \in \Gamma. \tag{22}$$

The potential U_1 is the solution of the Poisson equation within the magnetic particles and equals zero outside the magnets. At the surface of the magnets natural boundary conditions hold. The potential U_2 satisfies the Laplace equation everywhere

$$\triangle U(\boldsymbol{r}) = 0 \quad \text{for } \boldsymbol{r} \in \Omega_{\text{int}} \cup \Omega_{\text{ext}}, \tag{23}$$

with the following boundary conditions for $\boldsymbol{r} \in \Gamma$

$$U_2^{\text{int}} - U_2^{\text{ext}} = U_1, \tag{24}$$

$$\left(\nabla U_2^{\text{int}} - \nabla U_2^{\text{ext}}\right) \cdot \boldsymbol{n} = 0. \tag{25}$$

The potential U_2 shows a jump at the surfaces of the magnetic bodies.

The closed boundary value problem (20)–(22) can be solved using a standard finite element method. Both the potential U_1 and the direction cosines of the magnetic polarization, b_i, are interpolated by piecewise linear functions on a tetrahedral finite element grid. The resulting linear equation is solved using a conjugate gradient method with relaxed incomplete factorization (RILU) preconditioning [13]. During time integration of the LLG equation, the iterative solver can be started with the previous solution for U_1 as initial guess. Typically about 25 iterations are required in a system with 2×10^4 nodes. The equations (23)–(25) define a double layer potential

$$U_2(\boldsymbol{r}) = \frac{1}{4\pi} \int_\Gamma U_1(\boldsymbol{r}') \nabla' \frac{1}{|\boldsymbol{r} - \boldsymbol{r}'|} \cdot \boldsymbol{n}' \mathrm{d}r'^2 \tag{26}$$

which is created by a dipole sheet with magnitude U_1. In principle U_2 can be evaluated everywhere within the magnetic bodies using (26). However, instead of the direct computation of U_2 discretizing (26), we evaluate U_2 at the boundary and then we solve (23) within Ω_{int} using the known boundary values as Dirichlet conditions. To compute U_2 on Γ, we have to take the limit $\boldsymbol{r} \to \Gamma$ of the surface integral from inside Ω_{int}

$$U_2(\boldsymbol{r}) = \frac{1}{4\pi} \int_\Gamma U_1(\boldsymbol{r}') \nabla' \frac{1}{|\boldsymbol{r} - \boldsymbol{r}'|} \cdot \boldsymbol{n}' \mathrm{d}r'^2 + \left(\frac{\Omega(\boldsymbol{r})}{4\pi} - 1 \right) U_1(\boldsymbol{r}). \tag{27}$$

We discretize (27) using piecewise linear functions to interpolate U_1 on a triangular surface mesh. U_2 follows from a matrix vector product $\underline{U_2} = \mathbf{B}\underline{U_1}$. The boundary element matrix, $\mathbf{B}$, depends only on the geometry of the problem and has to be computed only once. $\mathbf{B}$ is a fully populated $m \times m$ matrix which relates the m boundary nodes with each other.

In summary we have to perform the following procedure to compute the demagnetizing field. Prior to the time integration of the LLG equation we

assemble the system matrices and compute an incomplete ILU factorization of the linear systems corresponding to equations (20) and (23). The setup phase also involves the computation of the boundary matrix **B**. Generally we are interested on the dynamic response of a system over a time span which is about two orders of magnitude larger than intrinsic precession time. Thus the CPU time of the setup phase is only a small fraction of the total CPU time. At each iteration during the time integration we have to perform the following steps to update the magnetostatic field:

1. Iterative solution of a linear system for U_1 (equation 20).
2. Matrix vector product to obtain U_2 at the boundary of the magnetic bodies (equation 27).
3. Iterative solution of a linear sytem for U_2 within the magnetic bodies (equation 23).
4. Sum U_1 and U_2 and build the gradient (equation 5).

3.2 Time integration

The precise understanding of the switching process of thin film nanomagnets is important for sensor and spin electronic applications. Surface irregularities and grain structure drastically change the reversal mechanism of thin film elements [14]. Taking into account surface roughness and grain structures requires an inhomogeneous computational grid which in turn causes very small time steps for time integration. Toussaint and co-workers [15] showed that the time step required to obtain a stable solution of the LLG equation with an explicit time integration scheme has to be proportional to $1/h^2$, where h is the size of the spatial grid. Edge roughness and an irregular grain structure may force small finite elements which leads to a small time step when an explicit time integration method is applied to solve the LLG equation. Yang and Fredkin [16] originally applied a BDF method in dynamic micromagnetic simulations. They apply the Galerkin variant of the finite element method for space discretization and a generalized minimum residual method (GMRES) to solve the linear systems involved in the solution process.

We use a collocation method to integrate the LLG equation (17) and assume that the equation is fulfilled at the nodes of the finite element mesh. Using spatial averaging we assign a magnetic moment

$$\boldsymbol{m}_i = \frac{1}{\mu_0} \int_{V_i} \boldsymbol{J}(\boldsymbol{r}) \mathrm{d}^3 r \tag{28}$$

to node i of the finite element mesh. The box volumes V_i have the following properties

$$\sum_{i=1}^{N} V_i = \int_{\Omega_{\mathrm{int}}} \mathrm{d}^3 r, \tag{29}$$

$$V_i \cap V_i = 0 \qquad \text{for} \quad i \neq j, \tag{30}$$

where the sum in (29) runs from 1 to the total number of nodes of the finite element mesh, N. The effective field at node i can be approximated as

$$\boldsymbol{H}^i_{\text{eff}} = -\frac{1}{\mu_0}\frac{\partial E_{\text{t}}}{\partial \boldsymbol{m}^i}. \tag{31}$$

Again a piecewise linear interpolation of the magnetic polarization vector on a tetrahedral finite element mesh is used to discretize the total magnetic Gibbs free energy, E_{t}.

Using (28) and (31) we can define a magnetic moment vector and an effective field vector at each node of the finite element mesh which leads to a system of $3N$ ordinary differential equations. It is solved using a BDF method [17]. Within the framework of this software package, the linear system at each Newton iteration is solved using a GMRES method. The GMRES method is a matrix free iterative method to solve a linear system of equations. Within the time integration package, the product of the Jacobian matrix times a vector is approximated using finite differences. Preconditioning partly replaces the finite difference approximation with exact curvature information. We provide the parts of the Jacobian matrix which are associated with the magnetocrystalline anisotropy and the ferromagnetic exchange interactions. As the short range interactions are the major source of stiffness in micromagnetic simulations, we obtain a significant speed up while keeping the system matrix sparse. A nonlinear system of equations has to be solved at each time step which can be effectively solved using the Newton method. Typically only 1–2 Newton steps are required to obtain convergence. However, the linear system to be solved at each Newton step may be ill-conditioned so that most of the total CPU time is spent in solving this system. A twofold procedure helps to speed up the calculation by more a factor of 40.

1. We provide an approximate Jacobian containing the short range interactions. This information is used to apply a left preconditioner to the internal matrix free GMRES solver of the time integration software.
2. The auxiliary linear equation which has to be solved for preconditioning of the internal GMRES solver is solved iteratively using a biconjugate gradient stabilized (BICSTAB) algorithm [18]. Among various preconditioners the imcomplete factorization (ILU) preconditioning proved to be most efficent for this auxiliary systems of linear equations.

3.3 Adaptive meshing

The numerical treatment of magnetization processes involves a wide range of length scale. A sufficiently fine finite element mesh is required to accurately predict the switching field of magnetic particles. Numerical experiments by Rave and co-workers [20] showed that the accurate simulation of the nucleation of reversed domains requires a mesh size comparable with the characteristic length of the material. As the mesh size reaches the critical length the

exchange energy density and the magnetostatic energy density balance each other and the nucleation field becomes independent of the grid spacing. The critical length scale depends on the relative strength of the exchange energy density with respect to the other micromagnetic energy terms. In soft magnetic materials the most dominant energy contribution is the magnetostatic energy. The significant length is given by the exchange length

$$l_{\mathrm{ex}} = \sqrt{\frac{2\mu_0 A}{J_{\mathrm{s}}^2}}. \tag{32}$$

In hard magnetic materials the most dominant energy contribution is the magneto-crystalline anisotropy energy. The significant length is given by the Bloch parameter

$$\delta_0 = \sqrt{\frac{A}{K_{\mathrm{u}}}}. \tag{33}$$

The typical length scales involved are the following:

- The typical sample size is in the range of micrometer range. Examples are the length of magnetic-nanowires or the lateral extension of magnetic thin film elements as used for sensor or storage elements [4].
- Most magnetic materials exhibit a polycrystalline structure. The grain size of magnetic thin film elements is in order of 10 nm [19].
- The characterstic length is an intrinsic property an is typically in the range from 3 nm – 5 nm. It is the length scale on which the magnetic polarization vector changes its direction [20].

Adaptive refinement and coarsening schemes are applied in order to scope with these different length scale in micromagnetic simulations. Hertel and Kronmüller [21] introduced an adaptive refinement scheme in static micromagnetic simulations, to calculate domain configurations in thin film elements. Here present a scheme to refine and coarse the mesh during the time integration of the LLG equation.

The general outline of adaptive algorithms is as follows. Starting from an initial triangulation τ_0, we produce a sequence of refined grids τ_{k}, until the estimated error is below a given tolerance ε. The nature of the micromagnetic problem allows to define a cheap a posteriori error indicator. Using piecewise linear function to represent the direction cosines of the magnetic polarization, the constraint (2) can only be hold at the nodal points of the finite element mesh. Thus an error indicator for the element e may be constructed by

$$\eta_e = \int_{\Omega_e} \left| \frac{\boldsymbol{J}\cdot\boldsymbol{J}}{J_{\mathrm{s}}^2} - 1 \right| \mathrm{d}^3 r / V_e. \tag{34}$$

The mesh is adjusted to the current magnetization distrubution during the solution of the LLG equation. We start with an initial triangulation τ_0. The mesh is refined in regions with non-uniform magnetization, whereas elements

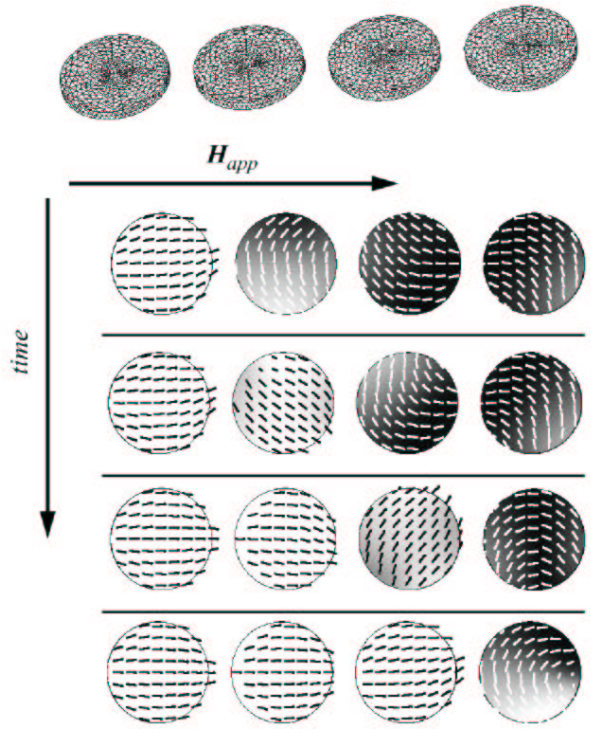

Fig. 1. Top: Surface of the finite element mesh of interacting NiFe nano-dots. Bottom: Time evolution of the magnetization pattern under the influence of an applied field

are taken out where the magnetization is uniform. After each time step we compute the error indicators. Depending on the distribution of the error indicators one of the following three procedures are applied:

Refinement. The error indicator of at least one element exceeds the global error tolerance ε. The time step is rejected. The mesh is refined in regions with high η_e. The previously accepted magnetization distribution is interpolated on the new nodes.

Coarsening. A certain percentage of elements shows an error indicator below a certain threshold, $\sigma\varepsilon$, with $\sigma < 1$. The time step is rejected and the current magnetization distribution is interpolated on the initial mesh, τ_0.

Proceed in time. Otherwise the time step is accepted and the time integration continues with the given grid.

The above algorithm guarantees that the simulation proceeds in time only if the space discretization error is below a certain threshold. Simulations of wall motion in nanowires show [22] showed that this adaptive scheme reduces the total CPU time by more than a factor of 4 as compared to a uniform mesh.

4 Examples

4.1 Magnetostatic interactions between circular nanodots

Circular magnetic nano-dots may be the basic structural units of future magnetic logic devices [23]. A critical parameter of these magnetic structures is the switching speed. As magnetization switching is induced by the magnetostatic interaction field of switched neighboring dots, the switching behavior is governed by the strength of the magnetostatic interactions and the nonuniform magnetization distribution during within the individual dots during the magnetization reversal process. Fig. 1 shows the finite element mesh (top) and the time evolution of the magnetization pattern (bottom) of interacting magnetic nano-dots. The diameter of the dots is 110 nm and their thickness is 10 nm. The intrinsic magnetic properties of permalloy were used for the simulations. The reversal time per dot is about 0.5 ns for an applied field of 5.6 kA/m using a Gilbert damping constant $\alpha = 0.1$. The magnetostatic interactions between the dots cause a dot by dot reversal of the chain. The magnetization of neighboring dots rotates in opposite directions, forming partial flux closure structures during the reversal process.

4.2 Surface roughness in magnetic nanoelements

Magnetic nano-elements have important applications as magnetic field sensors and might be used in future discrete storage media. A well defined switching field and a predictable domain structure are important prerequisites for the application of thin film elements. However, both the switching field and the switching time were found to depend strongly on the physical structure of the elements such as the surface roughness and the polycrystalline grain structure. In the following the switching process is compared for three different Co elements. One element denoted by (A) consists of a perfect microstructure. The surface is flat, no grains are assumed within the particle and the crystalline anisotropy is zero. Element (B) takes account of surface roughness. The notches are in average 8 nm. Element (C) consists of 500 columnar grains (diameter is 8 nm) with random distribution of the magnetocrystalline anisotropy directions. All the elements are 400 nm long, 80 nm wide and 25 nm thick. The granular element (C) has the largest coercive field, $H_c = 72$ kA/m. The coercive field decreases by less than 10 % for the perfect Co-element without crystalline anisotropy. Surface roughness leads to a reduction of the coercive field of about 20%. Fig. 2 shows the onset of magnetization reversal for the different elements under the influence of a reverse field of 100 kA/m. The switching time decreases from 0.75 ns for element (A) to 0.5 ns for element (C). Again a Gilbert damping constant $\alpha = 0.1$ was used. Fig. 3 shows the effect of preconditioning on the time integration error,

$$\eta_{\text{time}} = max_i |1 - \boldsymbol{J} \cdot \boldsymbol{J} / J_s^2|, \tag{35}$$

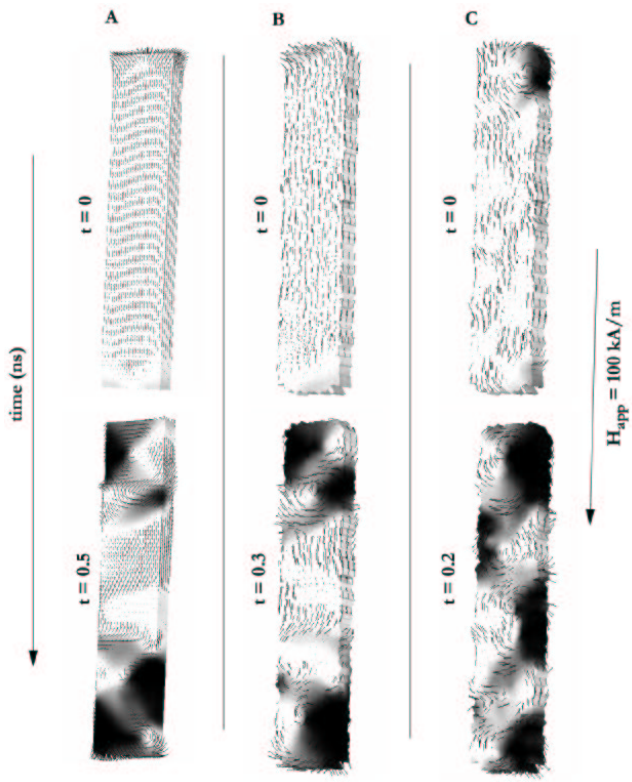

Fig. 2. Influence of the physical structure on the magnetization reversal of Co nano-elements. The plots compare the time evolution of (A) a flat element, (B) an element with surface roughness, and (C) an element with surface roughness and polycrystalline grain structure. Top row: Remanent magnetization distribution for zero applied field. Bottom row: Transient magnetic states during irreversible switching under the influence of a field of 100 kA/m . The component of the magnetic polarization is color coded. White: $\boldsymbol{J}$ antiparallel to $\boldsymbol{H}_{\mathrm{app}}$, black: $\boldsymbol{J}$ parallel to $\boldsymbol{H}_{\mathrm{app}}$

where i runs over all the nodes of the finite element mesh. The BDF solver without preconditioning does not preserve the norm of the magnetic polarization vector at the nodes of the mesh. Several renormalization steps of $\boldsymbol{J}$ are required during the time integration of the LLG equation. Preconditioning keeps the time discretization error small.

4.3 Domain wall motion magnetic nano-wires

The domain wall motion has been calculated in Co nano-wires as a function of the wire thickness. The thickness is varied in the range from 10 nm to 40 nm. The length of the wire is 600 nm. Initially, a reversed domain is created in one end. Under the influence of an applied field the domain with

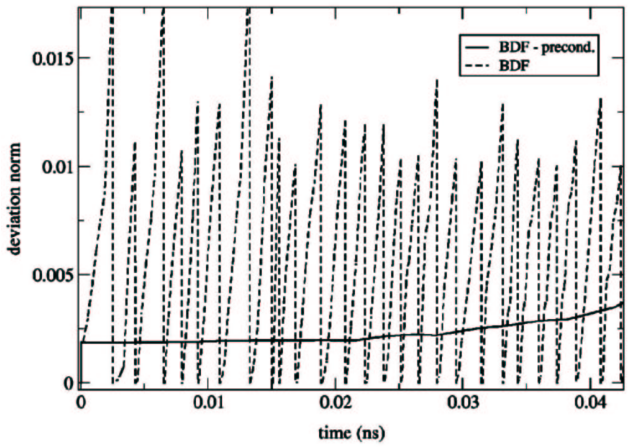

Fig. 3. Comparison of the time discretization error, η_{time}, for the integration of the LLG equation for sample (C) using a BDF method and a preconditioned BDF method

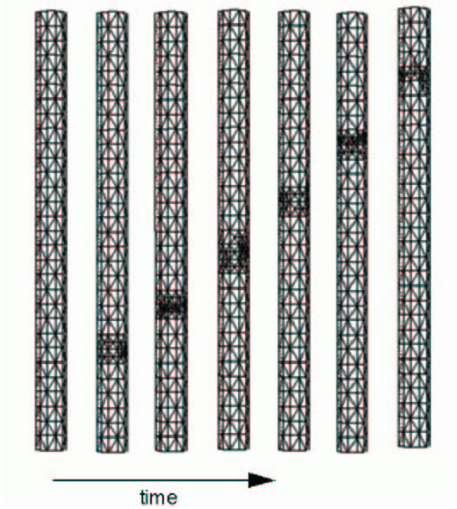

Fig. 4. Sequence of meshes during the motion of a domain wall in a magnetic nanowire. The coarse mesh has a size of 20 nm. At the wall position the mesh size is about 4 nm

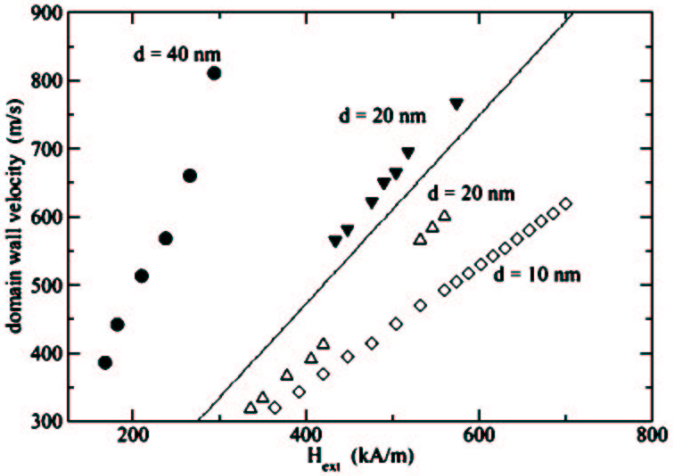

Fig. 5. Domain wall velocity as a function of the applied field for different diameters, d of the Co wire. For $d < 20$ nm transverse walls occur, for $d > 20$ nm vortex walls are energetically more favorable. Both types are found at $d = 20$ nm

the magnetization parallel to the field direction expands and the domain wall moves through the wire. During this process the magnetization remains nearly uniform within the core of both domains. Thus it is sufficient to resolve only the magnetization transition in the domain wall and use a coarse finite element mesh within the domains. As the wall moves, the finite element mesh is adjusted to the current wall position. Fig. 4 gives a sequence of finite element meshes during wall motion. The structure of the domain wall has a strong effect on the wall velocity. Thin wires show a transverse wall which move slowly. In thick wires, a vortex can form within the wall which causes an increase in the wall velocity. Fig. 5 shows the calculated domain wall velocities as a function of the applied field.

Acknowledgement

Work supported by the Austrian Science fund (Y-132PHY,13260TEC).

References

1. Aharoni A. (1996) Introduction to the Theory of Ferromagnetism. Oxford University Press, New York
2. Dahlberg, E. D., Zhu, J. G. (1995) Micromagnetic Microscopy and Modeling. Physics Today **48**, 34–40
3. Schabes, M. E., Fullerton, E. E., Margulies, D. T. (2001) Theory of Antiferromagnetically Coupled Magnetic Recording Media. J. Appl. Phys., in press

4. Johnson, M. (2000) Magnetoelectronic memories last and last ... . IEEE Spectrum **37**, 33–40
5. Brown Jr., W. F. (1963) Micromagnetics, Interscience, New York
6. Kinderlehrer, D., Ma, L. (1994) Computational Hysteresis in Modeling Magnetic Systems. IEEE Trans. Magn. **30**, 4380–4382
7. He L., Doyle W. D. et al. (1996) High-speed switching in magnetic recording media. J. Magn. Magn. Mat. **155**, 6–12
8. Akagi F., Nakamura A. et al. (2000) Computer Simulation of Magnetization Switching Behavior in High-Data-Rate Hard-Disk Media Masukazu Igarashi, IEEE. Trans. Magn. **36**, 154–158
9. Harrell, R. W. (2001) Orientation dependence of the dynamic coercivity of Stoner-Wohlfarth particles. IEEE Trans. Magn. **37**, 533–537
10. Gilbert, T. L. (1955)A Lagrangian formulation of gyromagnetic equation of the magnetization field, Phys. Rev. **100**, 1243
11. Chen, Q., Konrad, A. (1997) A review of finite element open boundary techniques for static and quasi-static electromagnetic field problems. IEEE Trans. Magn. **33**, 663–676
12. Fredkin, D. R., Koehler, T. R. (1990) Hybrid method for computing demagnetizing fields. IEEE Trans. Magn. **26**, 415–417
13. Bruaset, A. M. (1997) Krylov subspace iterations for sparse linear systems. In: Morten Daehlen, M., Tveito, A. (Eds.) Numerical Meth and Software Tools in Industrial Mathematics. Birkhauser, Boston, 21
14. Gadbois, J., and Zhu, J. G. (1995) Effect of Edge Roughness in Nano-Scale Magnetic Bar Switching. IEEE Trans. Magn. **31**, 3802–3804
15. Toussaint, J. C., Kevorkian, B., Givord, D., and Rossignol, M. F. (1996) Micromagnetic Modeling of Magnetization Reversal in Permanent Magnets. In: Proceedings of the 9th International Symposium Magnetic Anisotropy and Coercivity In Rare-Earth Transition Metal Alloys, World Scientific, Singapore, 59–68
16. Yang, B., Fredkin, D. R. (1998) Dynamical micromagnetics by the finite element method. IEEE Trans. Magn. **34**, 3842–3852
17. Cohen, S. D., and Hindmarsh, A. C. (1996) CVODE, A Stiff/Nonstiff ODE Solver in C. Computers in Physics, **10** 138–143.
18. Saad, Y. (1996) Iterative methods for sparse linear systems, PWS Publishing Company, Boston
19. Kirk, K. J., Chapman, J. N., Wilkinson, C. D. W. (1997) Switching fields and magnetostatic interactions of thin film magnetic nanoelements. Appl. Phys. Lett. **71**, 539–541
20. Rave, W., Ramstock, K., Hubert, A. (1998) Corners and Nucleation in Micromagnetics. J. Magn. Magn. Mater. **183**, 329–333
21. Hertel, R., Kronmuller, H. (1998) Adaptive finite element mesh refinement techniques in three-dimensional micromagnetic modeling. IEEE Trans. Magn. **34**, 3922–3930
22. Schrefl T., Forster H. et al. (2001) Micromagnetic Simulation of Switching Events, In: Kramer, B. (Ed.) Advances in Solid State Physics 41. Springer, Berlin Heidelberg, 623-635
23. Cowburn, R. P., Welland, M. E. (2000) Room temperature magnetic quantum cellular automata, Science **287**, 1466–1458

Index